Opto-Electronic Advances

Supplementary information

June 2023, Vol. 6, No. 6

DOI: 10.29026/oea.2023.220072

Highly sensitive and stable probe refractometer based on configurable plasmonic resonance with nano-modified fiber core

Jianying Jing[1,2,3], Kun Liu[1,2,3]*, Junfeng Jiang[1,2,3], Tianhua Xu[1,2,3], Shuang Wang[1,2,3] and Tiegen Liu[1,2,3]

[1]School of Precision Instruments and Opto-Electronics Engineering, Tianjin University, Tianjin 300072, China; [2]Key Laboratory of Opto-Electronics Information Technology, Ministry of Education, Tianjin University, Tianjin 300072, China; [3]Tianjin Optical Fiber Sensing Engineering Center, Institute of Optical Fiber Sensing, Tianjin University, Tianjin 300072, China.

*Correspondence: K Liu, E-mail: beiyangkl@tju.edu.cn

This file includes:

Supplementary information for this paper is available at https://doi.org/10.29026/oea.2023.220072

Section 1: The calculation of the equivalent refractive index

A hybrid nano-modified fiber core can be produced by coating a dielectric layer (i.e., WSe_2 layer in our work) with high-complex refractive index on the surface of the bare silica core. The disassembly of the cylindrical surface in the fiber core allows the hybrid mechanism at each point to be explained by a two-layer structure[S1], as shown in Fig. S1(b). The characteristic matrix of the two-layer structure, which can be calculated as a continuous product of the characteristic matrix of a single layer, is given as follows:

$$\boldsymbol{M}=\begin{bmatrix} M_{11} & M_{12} \\ M_{21} & M_{22} \end{bmatrix}=\begin{bmatrix} \cos\delta_1 & (\mathrm{i}\sin\delta_1)/\eta_1 \\ \mathrm{i}\eta_1\sin\delta_1 & \cos\delta_1 \end{bmatrix}\begin{bmatrix} \cos\delta_2 & (\mathrm{i}\sin\delta_2)/\eta_2 \\ \mathrm{i}\eta_2\sin\delta_2 & \cos\delta_2 \end{bmatrix}, \tag{S1}$$

where δ_r and η_r (r=1,2) represent the phase thickness and the oblique optical admittance of each layer, respectively. Each element in the matrix is expressed in Eq. (S2):

$$\begin{cases} M_{11}=\cos\delta_1\cdot\cos\delta_2-\sin\delta_1\sin\delta_2\dfrac{\eta_2}{\eta_1} \\ M_{12}=\dfrac{\mathrm{i}\eta_1\cos\delta_1\sin\delta_2+\mathrm{i}\eta_2\sin\delta_1\cos\delta_2}{\eta_1\eta_2} \\ M_{21}=\mathrm{i}\eta_1\sin\delta_1\cos\delta_2+\mathrm{i}\eta_2\cos\delta_1\sin\delta_2 \\ M_{22}=\cos\delta_1\cos\delta_2-\sin\delta_1\sin\delta_2\dfrac{\eta_1}{\eta_2} \end{cases}. \tag{S2}$$

The characteristic matrix of the hybrid layer formed by the two layers has the same form as that of the single layer, as expressed by Eq. (S3):

$$\boldsymbol{M}=\begin{bmatrix} M_{11} & M_{12} \\ M_{21} & M_{22} \end{bmatrix}=\begin{bmatrix} \cos\Gamma & (\mathrm{i}\sin\Gamma)/E \\ \mathrm{i}E\sin\Gamma & \cos\Gamma \end{bmatrix}. \tag{S3}$$

Each element in the matrix is given as follows:

$$\begin{cases} M_{11}=M_{22}=\cos\Gamma \\ M_{12}=(\mathrm{i}\sin\Gamma)/E \\ M_{21}=\mathrm{i}E\sin\Gamma \end{cases}. \tag{S4}$$

Therefore, the equivalent admittance E of the hybrid layer can be expressed in Eq. (S5):

$$E=\sqrt{M_{21}/M_{12}}=\sqrt{\frac{\eta_1\sin\delta_1\cos\delta_2+\eta_2\cos\delta_1\sin\delta_2}{\eta_1\cos\delta_1\sin\delta_2+\eta_2\sin\delta_1\cos\delta_2}\cdot\eta_1\eta_2}, \tag{S5}$$

where the phase thickness and the oblique optical admittance corresponding to s-polarized wave and p-polarized wave are described as follows:

$$\delta_r=(2\pi/\lambda)d_r(n_r^2-k_r^2-n_0^2\sin^2\theta_0-2\mathrm{i}n_rk_r)^{1/2}, \tag{S6}$$

$$\begin{cases} \eta_{rs}=\zeta(n_r^2-k_r^2-n_0^2\sin^2\theta_0-2\mathrm{i}n_rk_r)^{1/2} \\ \eta_{rp}=\dfrac{y_r^2}{\eta_{rs}}=\dfrac{\zeta^2(n_r-\mathrm{i}k_r)^2}{\eta_{rs}} \end{cases}, \tag{S7}$$

where $y_r=(n_r-\mathrm{i}k_r)\,\zeta$ is the characteristic optical admittance of the dielectric. ζ is the optical admittance in free space. The incident angle θ_r of the light in each layer can be calculated by Snell's law:

$$N_0\sin\theta_0=N_r\sin\theta_r, \tag{S8}$$

where $N_r=n_r-\mathrm{i}k_r$. N_r, n_r and k_r refer to the complex refractive index, the refractive index and the extinction coefficient of each layer, respectively.

In order to simplify the calculation, the incident angle is set as a constant value, and the refractive index of the bare fiber core is set as 1.4580 corresponding to the wavelength of 600 nm. For the conventional fiber plasmonic resonance sensor constructed by coating an Au layer on the surface of the bare fiber core, the slope of the wavevector component of the evanescent wave is calculated as 0.6964, and the resonance occurs at 618.22 nm. As shown in Fig. S1(a) the re-

fractive index of the WSe_2 layer ranges from 2.8075 to 4.5306 corresponding to the wavelength of 300 nm–1500 nm. The equivalent refractive index of the hybrid nano-modified fiber core is in the range from 1.4687 to 1.5174 which is higher than that of the bare fiber core, as seen in Fig. S1(b). For the NMF-CPR sensor constructed by coating an Au layer on the surface of the WSe_2-modified fiber core, the slope of the wavevector component of the evanescent wave ranges from 0.6692 to 0.6914, and the resonance wavelength is in the range of 519.61 nm–594.66 nm, as seen in Fig. S1(c) and S1(d), respectively. This exhibits obvious blueshift compared to that of the conventional fiber plasmonic resonance sensor. The comparison of the resonance wavelength of the sensors based on four types of TMDCs-modified fiber core is listed in Table S2. The peak refractive index corresponds to the minimum resonance wavelength that can be excited. The larger the peak refractive index, the smaller the minimum resonance wavelength.

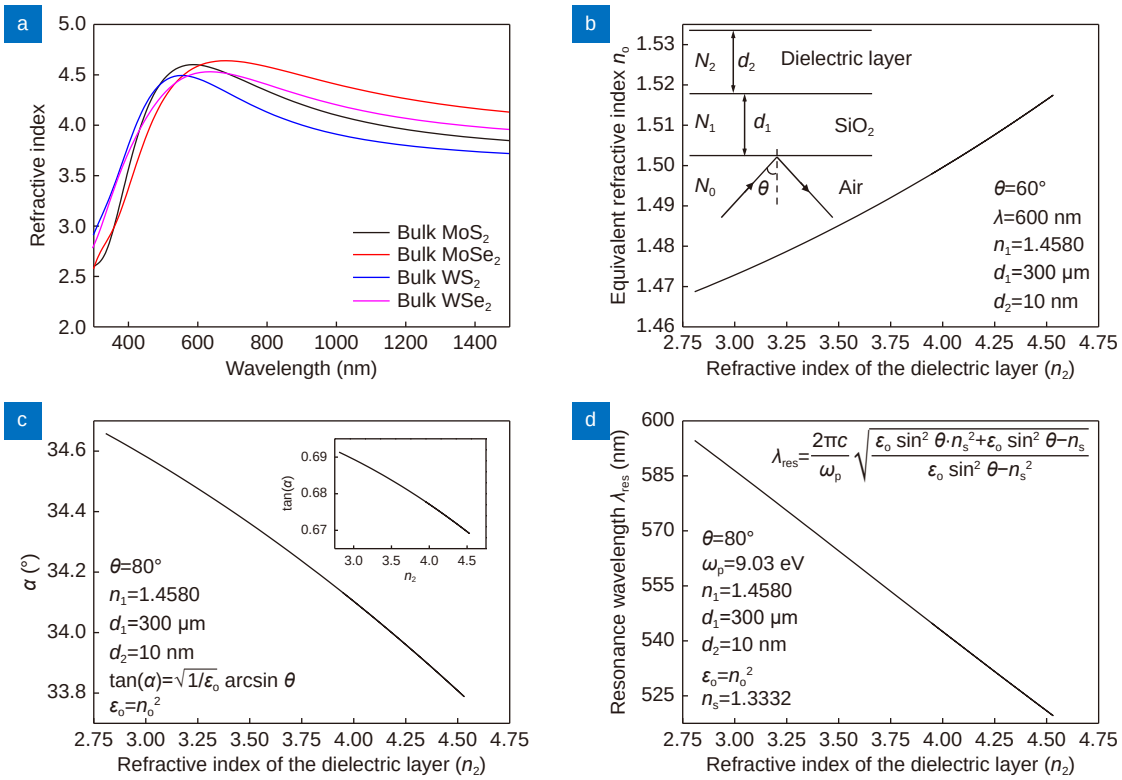

Fig. S1 | (**a**) Refractive index of four types of TMDCs. (**b**) The variation of the equivalent refractive index n_o with that of the dielectric layer n_2. Inset: the bilayer structure representing the hybrid nano-modified fiber core. θ and λ are the incident angle and the wavelength of the incident light, respectively. n_1 is the refractive index of the fiber core. d_1 and d_2 are the thicknesses of two layers, respectively. (**c**) The variation of the slope of the evanescent wave wavevector component with the refractive index of the dielectric layer n_2. (**d**) The variation of the resonance wavelength with the refractive index of the dielectric layer n_2. ω_p and n_s are the plasma frequency of Au and the refractive index of the sample layer, respectively.

Table S1 | Comparison of Hall effect measurement of four types of TMDCs under the same conditions.

TMDCs	Temperature (K)	Resistivity (Ω·cm)	Carrier mobility ($cm^2V^{-1}S^{-1}$)	Carrier concentration ($1/cm^3$)	Hall coefficient (cm^3/C)[a]	*f*-factor
MoS_2	300	1.76×10^4	6.44	5.52×10^{13}	-1.13×10^6	9.44×10^{-1}
$MoSe_2$		1.44×10^4	4.57	9.54×10^{13}	-6.55×10^5	9.15×10^{-1}
WS_2		7.73×10^2	12.9	6.27×10^{14}	-9.96×10^4	9.94×10^{-1}
WSe_2		1.21×10^2	30	1.72×10^{15}	-3.63×10^3	9.97×10^{-1}

[a] The negative Hall coefficient represents the N-type carrier.

Table S2 | Comparison of the resonance wavelength of the sensors based on four types of nano-modified fiber core.

Type of sensor	Refractive index of TMDCs (300 nm–1500 nm)	Equivalent refractive index of the nano-modified core	Slope of the wavevector component of the evanescent wave (tan*α*)	Resonance wavelength (nm)
Bare fiber core/Au	–	1.4580	0.6964	618.22
MoS_2–modified core/Au	2.6027–**4.6014**	1.4646–**1.5200**	**0.6680**–0.6933	**516.62**–603.21
$MoSe_2$–modified core/Au	2.6067–**4.6401**	1.4647–**1.5215**	**0.6674**–0.6932	**514.99**–603.05
WS_2–modified core/Au	2.9097–**4.4938**	1.4709–**1.5161**	**0.6697**–0.6903	**521.18**–590.30
WSe_2–modified core/Au	2.8075–**4.5306**	1.4687–**1.5174**	**0.6692**–0.6914	**519.61**–594.66

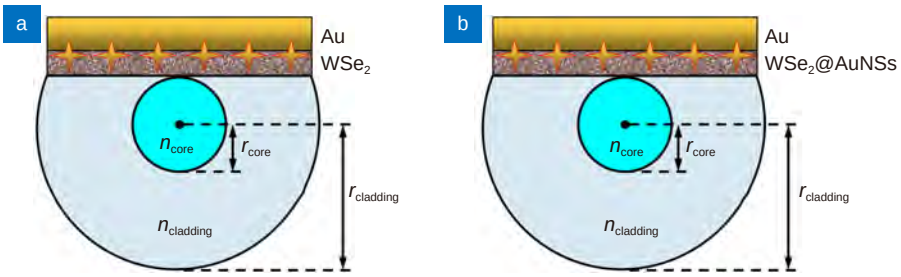

Fig. S2 | Schematic of the SPF based FEA models of (**a**) the NMF-CPR sensor and (**b**) the tip hot spot enhanced NMF-CPR sensor.

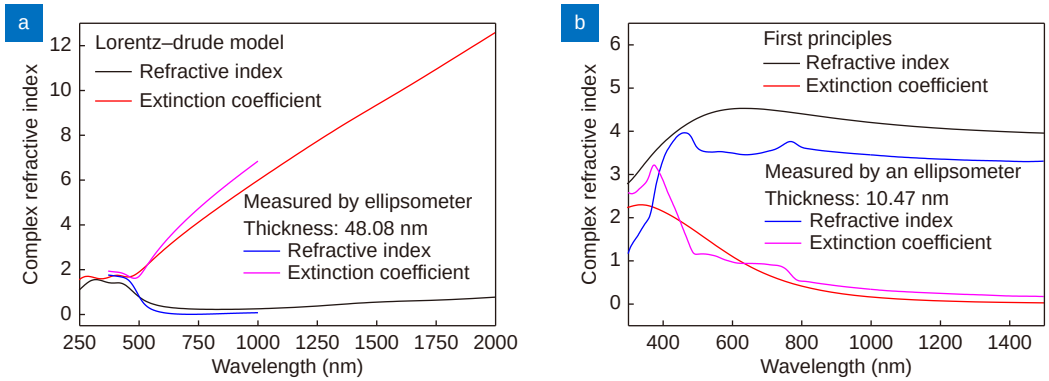

Fig. S3 | Complex Refractive indices of (**a**) the Au layer and (**b**) the bulk WSe_2. The variation of the measured curve is similar to that of the simulated curve, and the measured values are used for comparison only.

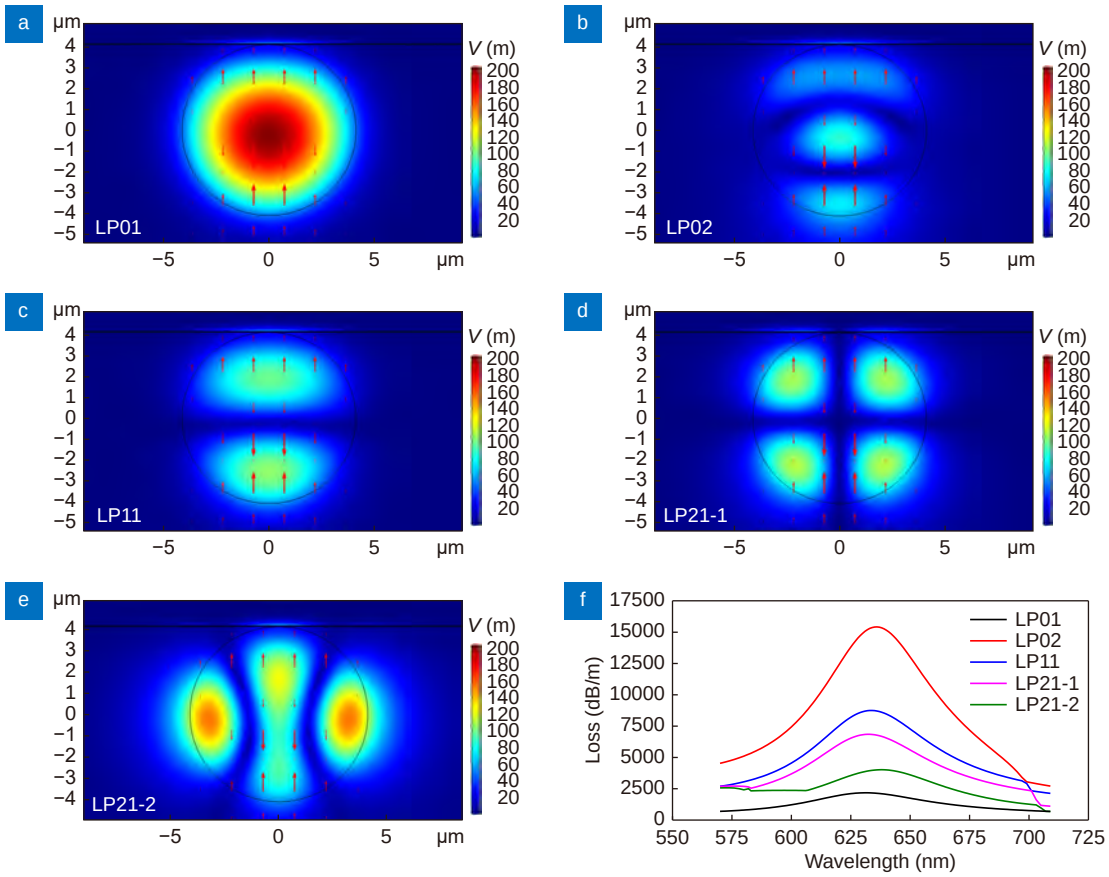

Fig. S4 | Mode field distributions of the (**a**) fundamental mode LP01 and (**b**–**e**) four higher-order modes LP02, LP11, LP21-1 and LP21-2. The darker the color in the mode field, the higher the energy. The red upward arrows represent the electric field that excites the plasmonic resonance. (**f**) Loss spectra corresponding to the fundamental mode LP01 and four higher-order modes LP02, LP11, LP21-1 and LP21-2.

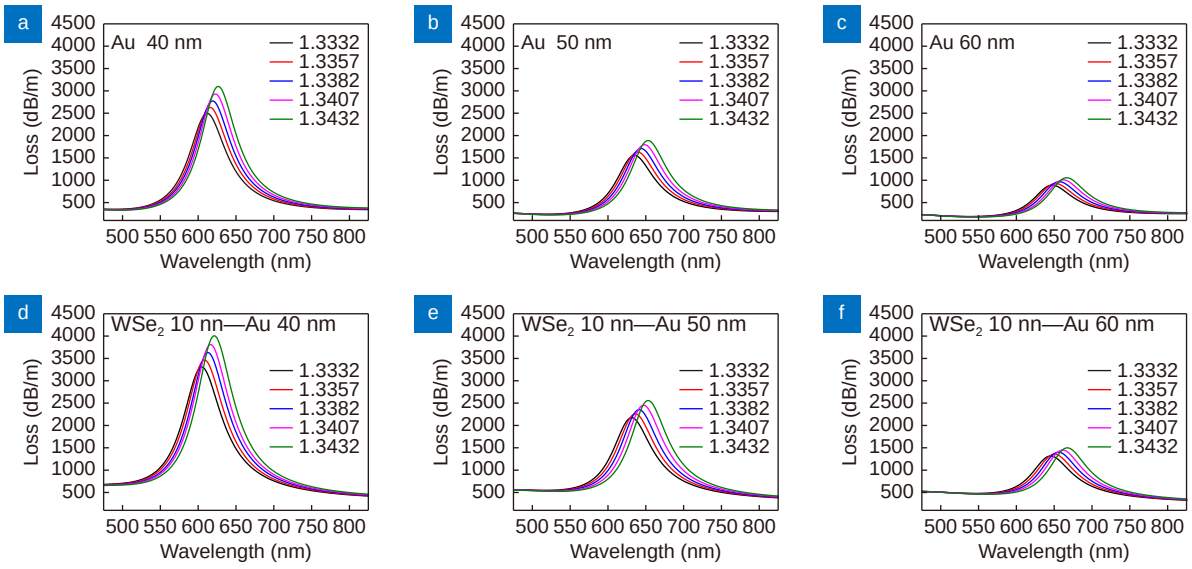

Fig. S5 | (**a**–**c**) Loss spectra of conventional fiber plasmonic resonance sensors with different thicknesses of Au layers. (**d**–**f**) Loss spectra of NMF-CPR sensors with different thicknesses of Au layers.

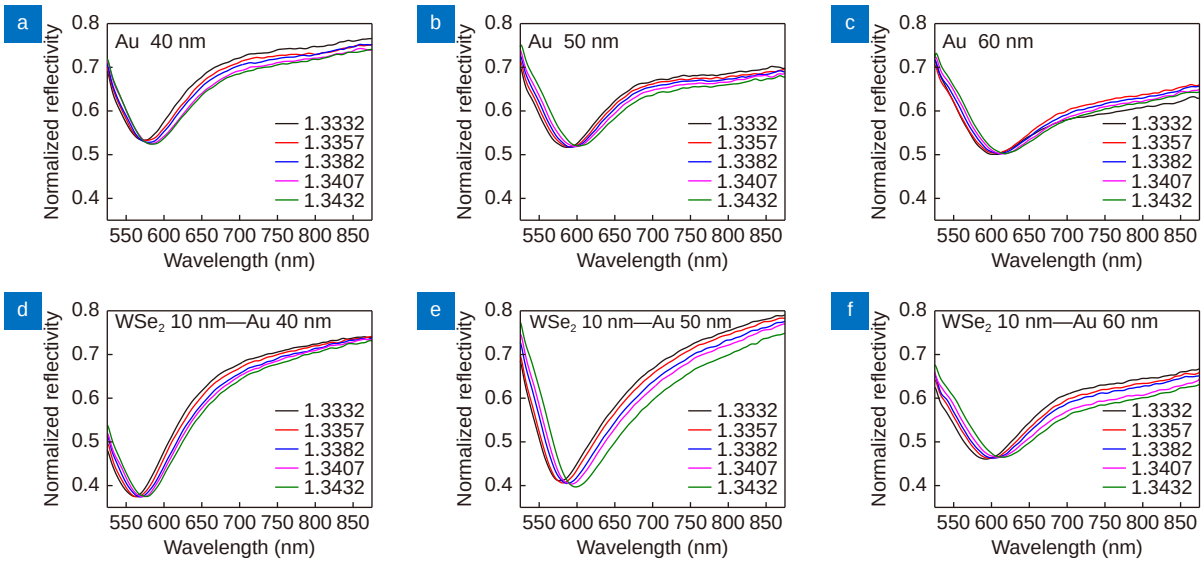

Fig. S6 | (**a**–**c**) Resonance spectra of conventional fiber plasmonic resonance sensors with different thicknesses of Au layers. (**d**–**f**) Resonance spectra of NMF-CPR sensors with different thicknesses of Au layers.

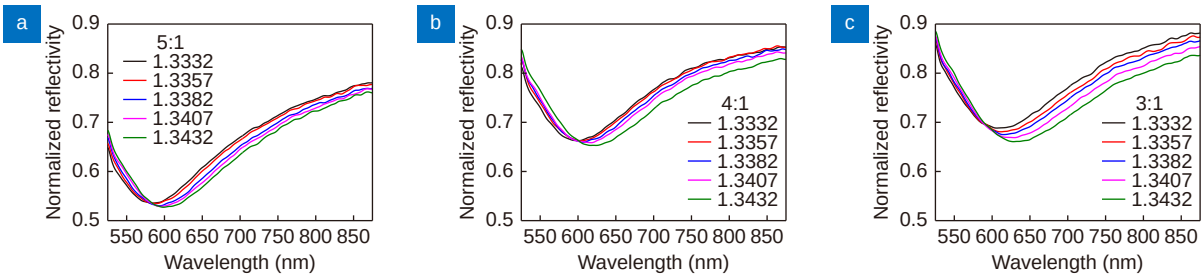

Fig. S7 | Resonance spectra of tip hot spot enhanced NMF-CPR sensors with different doping proportions (WSe_2 : AuNSs) of (a) 5 : 1, (b) 4 : 1 and (c) 3 : 1.

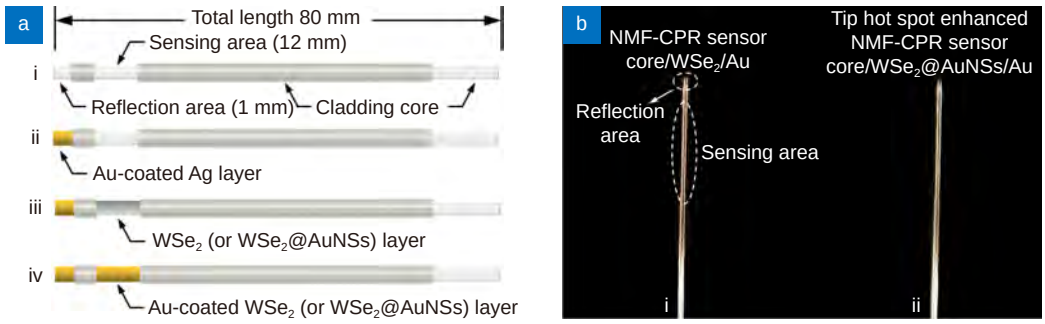

Fig. S8 | (**a**) Schematic of NMF-CPR sensors at each fabrication stage: i stripping of the cladding and grinding of the end face, ii sputtering of the Au-coated Ag layer on the surface of the reflection area, iii coating of the intermediate layer on the surface of the sensing area, iv sputtering of the Au layer on the sensing area. (**b**) Realistic images of i the NMF-CPR sensor and ii the tip hot spot enhanced NMF-CPR sensor.

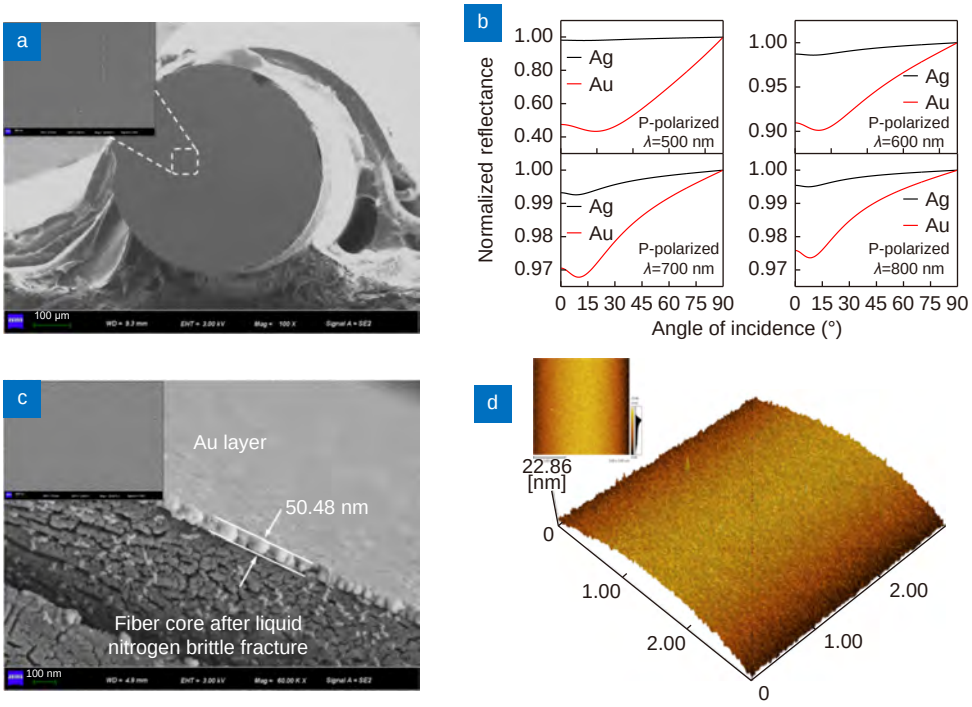

Fig. S9 | (**a**) SEM images of the end face of the bare fiber. (**b**) The reflectance of Ag and Au calculated based on the Fresnel's equation[S2]. (**c**) The SEM image of the sensing area cross section of the conventional fiber plasmonic resonance sensor with an Au layer of 50 nm. Inset: the SEM image of the surface of the conventional fiber plasmonic resonance sensor. (**d**) Atomic force microscope (AFM) images of the conventional fiber plasmonic resonance sensor, and the surface roughness of the Au layer is 3.75 nm.

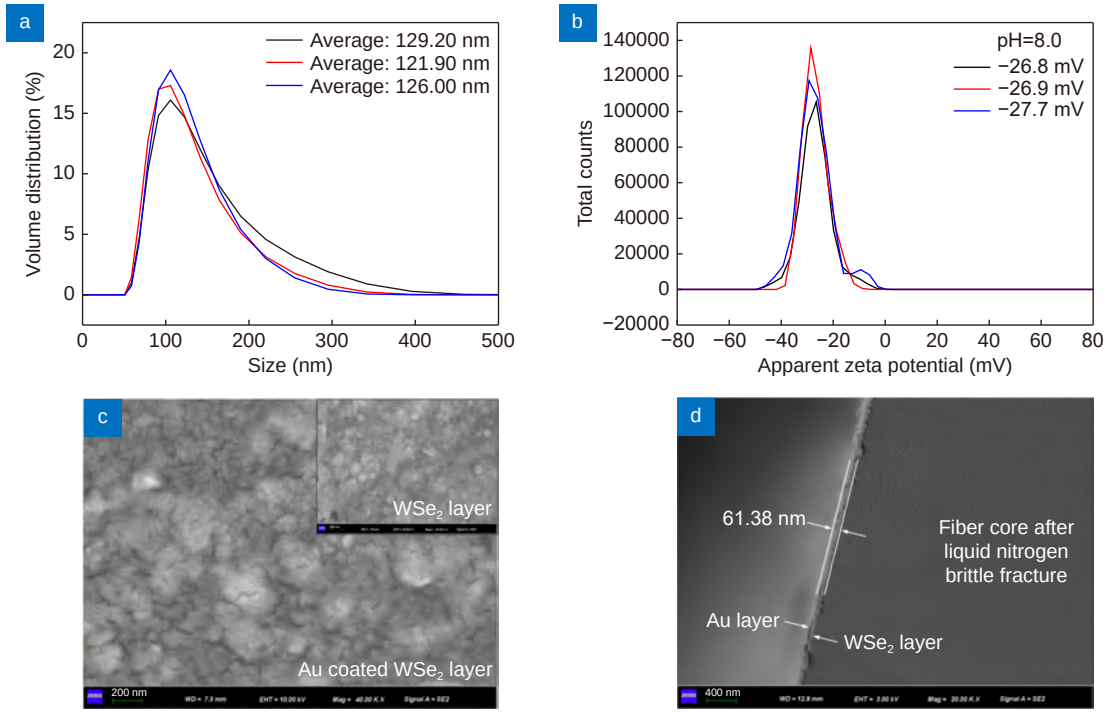

Fig. S10 | Three measurements of (**a**) Zeta potentials and (**b**) sizes of the ultrasonic-dispersed WSe_2 nanosheets. (**c**) The SEM image of the sensing area surface of the NMF-CPR sensor. Inset: WSe_2 nanosheets on the surface of the bare fiber. (**d**) The SEM image of the sensing area cross section of the NMF-CPR sensor.

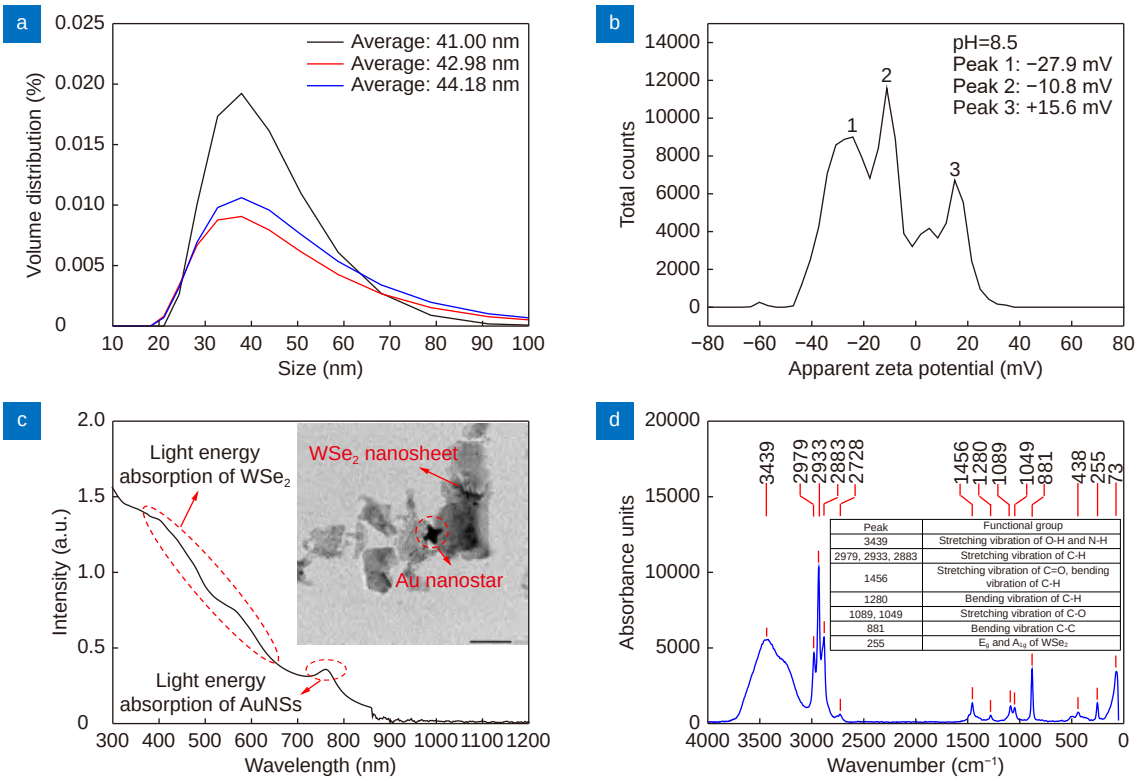

Fig. S11 | (**a**) Three measurements of sizes of AuNSs. (**b**) Single measurement of the Zeta potential of AuNSs dispersion. Peaks 1 and 2 represent Zeta potentials of alkaline dispersants, Peak 3 represents the Zeta potential of AuNSs. (**c**) UV-Vis absorption spectrum of the WSe_2@AuNSs. Inset: transmission electron microscope of the WSe_2@AuNSs. (**d**) The Raman spectrum of the WSe_2@AuNSs[S3−S9]. Hydroxyl groups exist on the surface of WSe_2 nanosheets, amino groups exist on the surface of AuNSs, and other functional groups exist in dispersants. There is no characteristic peak of Au.

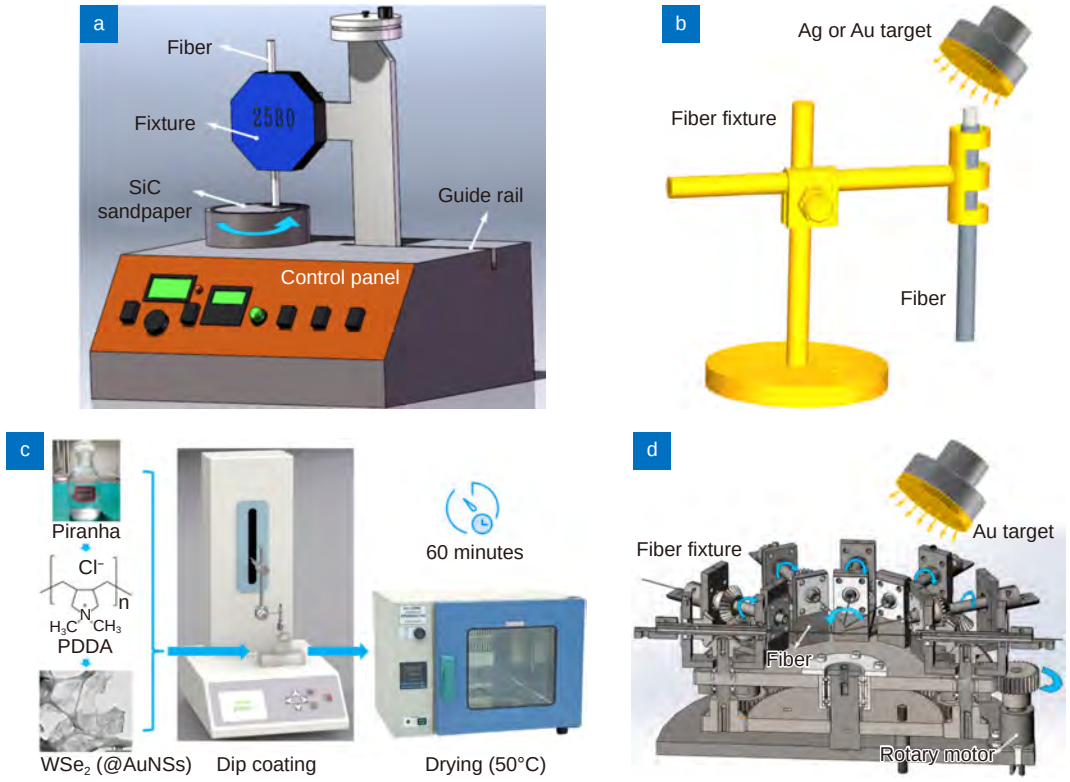

Fig. S12 | Schematic of fabrication processes of sensors. (**a**) The grinding of the end face of the fiber. (**b**) The sputtering of the Ag layer and the Au layer on the reflection area. (**c**) The coating of the WSe_2 layer (or the WSe_2@AuNSs layer) on the sensing area. (**d**) The sputtering of the Au layer on the sensing area.

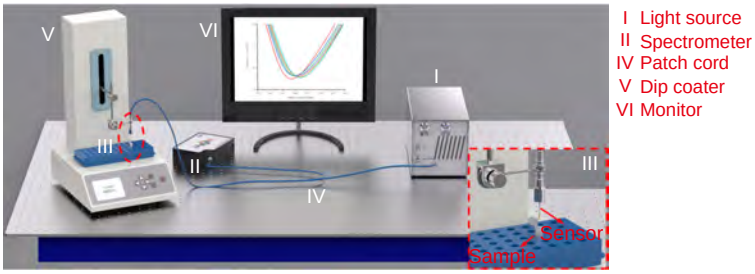

Fig. S13 | Schematic of the demodulation system.

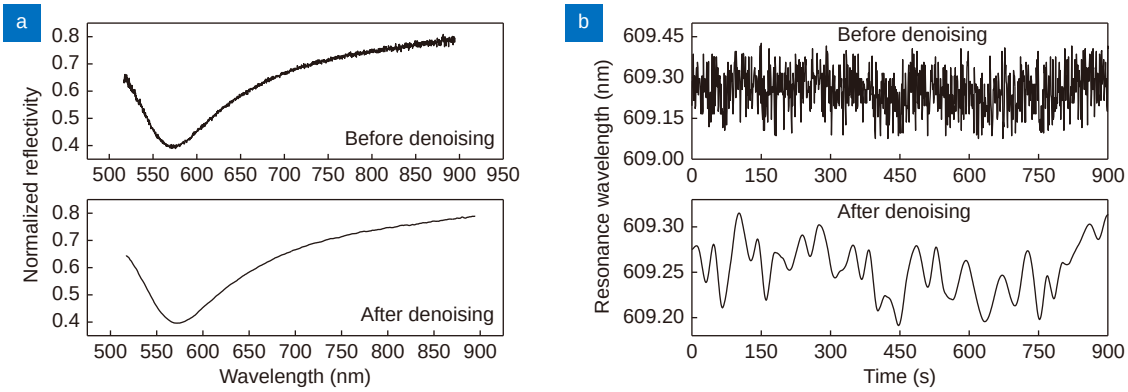

Fig. S14 | (**a**) The filtering of the spectral signal. (**b**) The real-time interrogation of the resonance wavelength.

Table S3 | Parameters for the simulation of spectral characteristics of sensors.

Structure	Refractive index	Size (nm)	Notes
Fiber core	$n_{\text{core}}(\lambda)=\sqrt{1+\frac{a_1\lambda^2}{\lambda^2-b_1^2}+\frac{a_2\lambda^2}{\lambda^2-b_2^2}+\frac{a_3\lambda^2}{\lambda^2-b_3^2}}$	Radius of the optical fiber core r_{core} = 4.1 μm	λ is the wavelength of the incident light. a_1, a_2, a_3, b_1, b_2 and b_3 are Sellmeier coefficients[S10].
Cladding	$n_{\text{cladding}}=\sqrt{{n_{\text{core}}}^2-NA^2}$	Radius of the optical fiber cladding r_{cladding} = 62.5 μm	Numerical aperture NA is 0.12.
Au layer	Lorentz–Drude model, as shown in Fig. S3(a). $n_{\text{Au}}=\sqrt{1-\frac{\Omega_p^2}{\omega(\omega-\mathrm{i}\Gamma_0)}+\sum_{j=1}^{k}\frac{f_j\omega_p^2}{(\omega_j^2-\omega^2)+\mathrm{i}\omega\Gamma_j}}$	Thickness 40 nm, 50 nm and 60 nm	ω is the angular frequency of the incident light. $\Omega_{\text{p}}=\sqrt{f_0}\omega_{\text{p}}$ is the plasmon frequency ω_{p} associated with intraband transitions with the oscillator strength f_0 and the damping constant Γ_0. k is the number of oscillators with the frequency ω_j, the strength f_j and the lifetime $1/\Gamma_j$[S11,S12].
WSe_2 layer	The calculation is based on the first principles, density functional theory and pseudopotential plane wave method[S13], as shown in Fig. S3(b).	Thickness 8 nm, 10 nm and 12 nm	In the fabrication of the NMF-CPR sensor, it is difficult to precisely control the number of layers of layered WSe_2 coated on the surface of the sensor, but it is easier to control the thickness of bulk WSe_2 Therefore, the simulation is based on the refractive index of bulk WSe_2 in order to achieve a good agreement with the subsequent experiments.

References

S1. Zhang XB, Luo H, Tan ZQ, Liu WB, Wu SY. Effects of small-scale surface roughness and absorption on refractive index measurement by the Brewster-angle and critical-angle techniques. *Acta Photonica Sin* **46**, 0412001 (2017).

S2. Zhu QF, Li PG, Gao N, Hu X, Li C et al. Deducing localized surface plasmon properties through analysis of the far-field optical spectra. *J Phys D Appl Phys* **55**, 015108 (2022).

S3. Wu JD, Zhou RY, Radjenovic PM, Liu S, Wu DY et al. Electrochemical impedance spectroscopy and Raman spectroscopy studies on electrochemical interface between Au(111) electrode and ethaline deep eutectic solvent. *Electrochim Acta* **390**, 138859 (2021).

S4. Cong TZ, Wang JZ, Zhao YP, Zhang DM, Fan Z et al. Tip-to-tip assembly of urchin-like Au nanostar at water-oil interface for surface-enhanced Raman spectroscopy detection. *Anal Chim Acta* **1154**, 338323 (2021).

S5. Ghule AV, Lo B, Tzing SH, Ghule K, Chang H et al. Simultaneous thermogravimetric analysis and in situ thermo-Raman spectroscopic investigation of thermal decomposition of zinc acetate dihydrate forming zinc oxide nanoparticles. *Chem Phys Lett* **381**, 262–270 (2003).

S6. Zhang Z, Huang LL, Sheng SC, Jiang CY, Wang YP. MIL-125(Ti)-derived COOH functionalized TiO_2 grafted molecularly imprinted polymers for photoelectrochemical sensing of ofloxacin. *Sensor Actuat B Chem* **343**, 130119 (2021).

S7. Xiao YJ, Wang T, Wang XQ, Gao XX. Surface-enhanced near-infrared Raman spectroscopy of nicotinamide adenine dinucleotides on a gold electrode. *J Electroanal Chem* **433**, 49–56 (1997).

S8. Nasu T, Ozaki Y, Sato H. Study of changes in water structure and interactions among water, CH_2, and COO^- groups during water absorption in acrylic acid-based super absorbent polymers using Raman spectroscopy. *Spectrochim Acta A Mol Biomol Spectrosc* **250**, 119305 (2021).

S9. Dos Santos EP, Silva FLR, Gontijo RN, Alves JM, Ammar MR et al. Temperature dependence of the double-resonance Raman bands in bilayer WSe_2. *Vib Spectrosc* **110**, 103117 (2020).

S10. Sharma AK, Rajan, Gupta BD. Influence of dopants on the performance of a fiber optic surface plasmon resonance sensor. *Opt Commun* **274**, 320–326 (2007).

S11. Ordal MA, Bell RJ, Alexander RW Jr, Long LL, Querry MR. Optical properties of fourteen metals in the infrared and far infrared: Al, Co, Cu, Au, Fe, Pb, Mo, Ni, Pd, Pt, Ag, Ti, V, and W. *Appl Opt* **24**, 4493–4499 (1985).

S12. Rakić AD, Djurišić AB, Elazar JM, Majewski ML. Optical properties of metallic films for vertical-cavity optoelectronic devices. *Appl Opt* **37**, 5271–5283 (1998).

S13. Gu GG, Song BK, Fang MS, Hong YL, Chen XG et al. Layer-dependent dielectric and optical properties of centimeter-scale 2D WSe_2: evolution from a single layer to few layers. *Nanoscale* **11**, 22762–22771 (2019).